International Journal of Science and Research (IJSR)
ISSN: 2319-7064
SJIF (2022): 7.942

Numerical Study of NACA0012: An Application of VAWT with CFD Tools

Sánchez, José M.[1], Ramírez Rafael[2], Garrido Jhonatan[3], Barreto Carlos[4]

[1, 2, 3]Universidad del Atlántico. Departamento de Ingeniería Mecánica, Carrera 30 Número 8 – 49, Puerto Colombia, Área Metropolitana de Barranquilla, Colombia

[4]University of Puerto Rico Mayaguez Campus. Chemical Engineering Department, Mayaguez, Puerto Rico.

Abstract: ***A significant increase of the energy generation techniques demands the application of computational resources to design the mechanical components and aerodynamic profiles of vertical axis wind turbines (VAWT) to analyze and improve their energy efficiency. For this reason, experimental studies have been conducted to analyze NACA 00-series with symmetric blades under low and high Re conditions. In this research, the shape of the NACA 0012 airfoil is formed in a 2D computational domain to solve the Navier-Stokes equations and analyze the behavior of the airflow around the surfaces of the airfoil with ANSYS Fluent solver. A mesh independence study determined an optimal number of 12005 cells and 12250 nodes to conform the structured mesh. On the other hand, the convergence criterion equal to 1_x10^{-5} and the fast data processing of structured meshes defined a regular grid to visualize the contours of the airflow velocity, the airflow pressure, and the turbulent kinetic energy for each angle of attack (AoA) of the airfoil. A good agreement between the numerical model and the experimental data demonstrated an efficient application of the CFD methodology to calculate the pressure coefficient, the drag coefficient, the lift coefficient, the pitching moment coefficient, and the Cl/Cd ratio with a high peak value close to AoA=10° for two Re equal to 17600 and 35200. A remarkable description of the flow wake generation was reached by the SKW, BSLKW, GEKOKW, SKE, and RKE with a better visualization of the vortex shedding between 10º to 20º AoA in the CFD model.***

Keywords: VAWT, RANS model, CFD Analysis, NACA 0012.

1. Introduction

Renewable energy resources and CFD techniques enhance the development of aerodynamic components with greater energy efficiency and lower manufacturing costs [1]. A considerable effort to understand and improve the efficiency limitations of the VAWT design facilitates the numerical analysis of the oscillation phenomenon produced by the interaction between a free airflow and an airfoil geometry [2].

The numerical analysis can satisfy the needs of the electrical energy consumption due to the intense industrialization. In this sense, the kinetic energy analysis of air streams is needed to study the best VAWT configuration and produce energy from renewable resources [3]. As seen by Parakkal et al. [4], where the Joukowski airfoil was investigated considering the cambered NACA 4312 and symmetrical NACA 0012 with the CFD methodology and the Panel method technique. The lift coefficient (Cl) validated the CFD method for an element size equal to 0.004 mm and 1.2 growth rate for an AoA range from -5º to 20º. The torque coefficient (Ct) and Tip Speed Ratio (TSR) were plotted to visualize a dominant performance of the Joukowski airfoil with Ct close to 0.75 for 10 TSR.

In view of the above, a greater effort to develop efficient wind turbines under low Re conditions to match the low-altitude wind speed is expressed through the CFD analysis to calculate the aerodynamic coefficients of NACA airfoils and generate a better insight of the performance of small-scale turbines in complex zones of the computational domain [5]. Yossri et al. [6] conducted a comprehensive CFD study to explore the effect of the airfoil section and the rotor diameter size on the power generation of a small-scale HAWT using the VOF method. The NS equations defined lift and drag forces for four airfoils: NACA 0012, NACA 4412, NACA 0015, and NACA 4415 and three rotor diameter sizes of 500mm, 750mm, and 1000mm. This numerical analysis showed the highest lift to drag ratio for the NACA 4412 airfoil and the power density of 11.011 W/m2 for1000mm rotor diameter.

Kulshreshtha et al. [7] analyze the airflow around three types of airfoils: NACA 2412, NACA 2414 and NACA 2415. The NS equations for steady state and the Standard k-ε model calculate the aerodynamic forces and the performance coefficients associated to the airfoil. Monitors of lift and drag coefficients verified the convergence supported by a second order scheme and the method pressure-velocity coupling [8]. The range(-5º to 20º)shown the NACA 2412 airfoil like the best geometry with the maximum lift/drag ratio equal to 27.9206 for 4º AoA, maximum Cd equal to 1.8 for 20° AoA and maximum Cl equal to 6.0614 for 19° AoA.

Maia et al.[9] studied a preconditioning-based approach to guarantee robustness and stability during the CFD solution of low Mach number flows [10]. The finite volume method (FVM) was applied to discretize the computational domain and solve the NS equations coupled to the Fluent solver [11], [12].As a result, the hexahedral mesh with 63180 cells showed the velocity and pressure contours from 0.1 to 1.2 Mach number.

The turbulence models are strongly used in the analysis of the turbulent kinetic energy (TKE) and dissipation rate to describe the vortex detachment and the shear stresses associated to the flow displacement around the airfoil[13], [14]. Liu and Nishino[15] performed a three-dimensional

simulation of the flow around the NACA0012 airfoil modifying the Re, AoA and the mesh resolution[16]. Results showed a relation between the oscillation of stall cells and the lift fluctuation with a variable span–wise mesh resolution of 10%, 5%, and 2.5% of the chord length.

In this paper, a mesh independence study is carried out to analyze the numerical results against the experimental study developed by Sengupta et al. [17].Re values of 17600 and 35200 were simulated to visualize the interaction between the flow velocity and the airfoil geometry with the aim to study the appropriate turbulence models to solve the NS equations and analyze the turbulence effects which may influence the performance coefficients associated to the airfoil geometry applied to VAWTs into the virtual environment.

2. Airfoil Geometry

A CAD tool modeled the NACA 0012 in form of the set of coordinates in the x, y plane and the main dimensions of the airfoil with the chord length (c) equal to 1 meter. The Eq. 1 defines the 0012 series which conform the airfoil [18].

$$y = 5t_{max}\, c\left[0.2969\left(\frac{x}{c}\right)^{1/2} + (-0.1260)\left(\frac{x}{c}\right) + (-0.3516)\left(\frac{x}{c}\right)^{2} + 0.2843\left(\frac{x}{c}\right)^{3} + (-0.1015\left(\frac{x}{c}\right)^{4}\right] \quad (1)$$

where the first digit of the NACA 0012 determines the maximum camber of the airfoil. The second number determines the distance of the maximum camber from the airfoil leading edge, third and fourth number represent the maximum thickness of the airfoil. In this sense, NACA 0012 is a symmetrical airfoil with a maximum thickness of 12%.

The coordinates of the airfoil NACA 0012 were selected due to the high application in the aerodynamic flow simulation of VAWTs, where a virtual environment shows the physical properties of the airflow validating the approximated solution of the partial differential equations reached with CFD tools.

The computational domain contains a semi-circular region with a diameter equal to 20c in the inlet and a rectangular region of 40c after the airfoil section, where the interaction between the airfoil and the airflow is discretized. This CFD method is based on the numerical discretization proposed by Brown et al.[14] where the structured mesh optimizes the number of cells needed to reach an efficient approximation in the solution of the NS equations. Fig. 1 shows the domain modeled with CAD tools, where an AoA from 0º to 90º influences the flow near to the surfaces of the NACA 0012 in each numerical simulation.

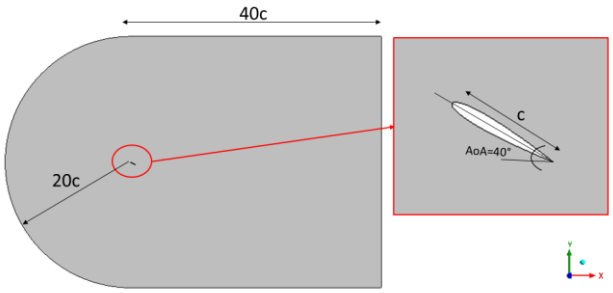

Figure 1: Computational domain of the CFD study.

3. Numerical model

The numerical analysis of the NS equations determines the complex problem solving in science, engineering, and technology for automotive, aeronautical, mechanical, electronics, oil & gas, chemical, aerospace, civil, environmental engineering, or bioengineering. ANSYS software may be used to improve the properties of wing sections for laminar or turbulent flows and describe the vortex detachment near to the surfaces of the airfoil. As presented by Bellakhal et al. [19] in the assessment of two equations turbulence models, the finite volume method (FVM) computes the NS equations for incompressible, laminar, and two-dimensional flows to simulate the streamlines around the airfoil and determine the performance coefficients for each thermodynamic state.

In this CFD simulation, the pressure-based algorithm predicts the main dependent variables with the application of the coupled scheme in second order. An iterative analysis determines the flow field and the inertial forces of the airflow through the solution of the conservation equations of mass, momentum, and energy expressed by the Eq. 2, Eq. 3, and Eq. 4 respectively [20].

$$\frac{\partial \rho}{\partial t} + \nabla \cdot \left(\rho \vec{V}\right) = 0 \quad (2)$$

$$\frac{\partial}{\partial t}\left(\rho \vec{V}\right) + \nabla \cdot \left(\rho \vec{V}\vec{V} + p\bar{\bar{I}}\right) - \nabla \cdot \bar{\bar{\tau}} = 0 \quad (3)$$

$$\frac{\partial}{\partial t}(\rho e) + \nabla \cdot \left(\rho h \vec{V}\right) - \nabla \cdot \left(\bar{\bar{\tau}} \cdot \vec{V} - \vec{q}\right) = 0 \quad (4)$$

On the other hand, Eq. 5 relates the kinetic energy with the pressure contours between the boundaries of the 2D computational domain. For each turbulence model, the convergence criterion equal to $1x10^{-5}$reached a stable solution and a good behavior of the residual values [21].

$$p = \rho(\Upsilon - 1)\left(e - \frac{V^2}{2}\right) \quad (5)$$

A set of computational treatments were necessary to reduce the instabilities and enhance the CFD model to obtain an appropriate numerical solution [22]. The mesh refinement technique improved the robustness in the CFD model enhancing the prediction of the complex turbulent flow close to the airfoil surfaces considering an AoA range from 0º to 90º. Seven turbulence models analyzed the flow phenomena around the airfoil with the modeling of the environmental VWAT conditions in Fluent solver: Standard k-ε (SKE), RNG k-ε (RNGKE), Realizable k-ε (RKE),

Standard k-ω (SKW), GEKO k-ω (GEKOKW), SST k-ω (SSTKW), and BSL k-ω (BSLKW).

3.1 Standard k-ε model

The physical effects of the turbulence phenomena are strongly associated with the Re number modeled into the computational domain. Therefore, a reliable CFD prediction involves an adequate simulation of the turbulence from the numerical model setup considering the temporal and spatial scales with a cost-effective approach. In accordance with the above, the standard k – ε model calculates the Reynolds stress terms for a wide range of industrial applications with the low computational cost required to define the turbulent kinetic energy and its dissipation rate (Eq. 6 and Eq. 7, respectively) [23].

$$\frac{\partial}{\partial t}(\rho k)+\frac{\partial}{\partial x_i}(\rho k u_i)=\frac{\partial}{\partial x_j}\left[\left(\mu+\frac{\mu_t}{\sigma_k}\right)\frac{\partial k}{\partial x_j}\right]+G_k-\rho\varepsilon \quad (6)$$

$$\frac{\partial}{\partial t}(\rho\varepsilon)+\frac{\partial}{\partial x_i}(\rho\varepsilon u_i)=\frac{\partial}{\partial x_j}\left[\left(\mu+\frac{\mu_t}{\sigma_\varepsilon}\right)\frac{\partial \varepsilon}{\partial x_j}\right]+C_{1_\varepsilon}\frac{\varepsilon}{k}G_k-C_{2_\varepsilon}\rho\frac{\varepsilon^2}{k} \quad (7)$$

where, Gk determines the turbulence kinetic energy production in form of the mean velocity gradients. $C_{1_\varepsilon}=1.44$ and $C_{2_\varepsilon}=1.92$ are constant values of the model. σ_k=1.0 and $\sigma_\varepsilon=1.3$ are the turbulent Prandtl numbers for k and ε values which are used in a wide range of flow transport processes and experimental studies [24].There is a continuous interest in the enhancement of the turbulence models and the computational cost reduction of two equation models, where the turbulent shear stresses are associated to the mean rate of strain, as shown in Eq. 8 [25].

$$-\rho\overline{u'v'}=\mu_t\frac{\partial u}{\partial x_j} \quad (8)$$

One of the most important features of the standard k-ε model is the assumption of the turbulent viscosity and the thermal diffusivity presented in Eq. 9 and Eq. 10.

$$\mu_t=\rho C_\mu\frac{k^2}{\varepsilon} \quad (9)$$

$$k_t=\frac{C_p\mu_t}{\sigma_k} \quad (10)$$

Cμ is equal to 0.09 and ε can be replaced by $\rho k^{\frac{3}{2}}/l$ considering the effects of the molecular viscosity for high Re numbers and the application of fine meshes near to the wall of the computational domain to improve thesimulation results.

3.2 RNG k-ε model

According to Kolmogorov[26], the turbulence is constituted by eddies with an amount of kinetic energy larger than the viscous dissipation. The RNG model calculates μ_t with a relatively low computational cost due to the application of the Boussinesq approach and the renormalization method. An additional term in Eq. 11 modifies the dissipation equation as follows [27].

$$\frac{\partial}{\partial t}(\rho\varepsilon)+\frac{\partial}{\partial x_i}(\rho\varepsilon u_i)=\frac{\partial}{\partial x_j}\left[\left(\mu+\frac{\mu_t}{\sigma_\varepsilon}\right)\frac{\partial \varepsilon}{\partial x_j}\right]+C_{1_\varepsilon}\frac{\varepsilon}{k}G_k-\rho\frac{\varepsilon^2}{k}\left(C_{2_\varepsilon}+\frac{C_\mu\eta^3\left(1-\eta/\eta_0\right)}{1+\beta\eta^3}\right) \quad (11)$$

where: $\eta\equiv\frac{Sk}{\varepsilon}$, $\eta_0=4.38$, $\beta=0.012$. RNGmodel considers these constant values for $C_\mu=0.0845$, $C_{1_\varepsilon}=1.42$, and$C_{2_\varepsilon}=1.68$ to improve the accuracy of the flow simulation.

3.3 Realizable k-ε model

This turbulence model predicts the behavior of the interacting flow around the complex surfaces of the computational domain in a control volume previously defined with high efficiency. The equations of the Realizable k-ε model are pre-coded to calculate the turbulence considering the energy needed to displace the flow in a velocity range from 1 m/s to 5 m/s. The turbulent kinetic energy (k) and the dissipation rate (ε) are variables expressed byEq. 12 andEq.13, respectively.

$$\frac{\partial}{\partial t}(\rho k)+\frac{\partial}{\partial x_j}(\rho k u_j)=\frac{\partial}{\partial x_j}\left[\left(\mu+\frac{\mu_t}{\sigma_k}\right)\frac{\partial k}{\partial x_j}\right]+G_k-\rho\varepsilon \quad (12)$$

$$\frac{\partial}{\partial t}(\rho\varepsilon)+\frac{\partial}{\partial x_j}(\rho\varepsilon u_j)=\frac{\partial}{\partial x_j}\left[\left(\mu+\frac{\mu_t}{\sigma_\varepsilon}\right)\frac{\partial \varepsilon}{\partial x_j}\right]+C_{1\varepsilon}\frac{\varepsilon}{k}G_k-C_{2\varepsilon}\rho\frac{\varepsilon^2}{k} \quad (13)$$

where:

$$C_{1\varepsilon}=\max\left[0.43,\frac{\eta}{\eta+5}\right],\eta=S\frac{k}{\varepsilon},S=\sqrt{2S_{ij}S_{ij}};\ C_{2\varepsilon}=1.9.$$

This CFD methodology complements the experimental analysis of the physical variables and describes the turbulent kinetic energy transferred between the surfaces of the airfoil. Realizable k-ε model presents a different formulation of the turbulent viscosity (μ_t) expressed in Eq. 14 as a variable with a significant influence over the predictability of the viscous flows.

$$\mu_t=\rho C_\mu\frac{k^2}{\varepsilon} \quad (14)$$

where C_μ determines the airflow into the control volume of the CFD study. For the Realizable model application, Eq. 15 determines flow changes in function of the constant values A_0, A_s, and the turbulent kinetic energy (k), as follows:

$$C_\mu=\frac{1}{A_0+A_S\frac{kV}{\varepsilon}} \quad (15)$$

A_0 is equal to 4.04 and A_s is equal to $\sqrt{6}\cos ø$. where:

$$ø=\frac{1}{3}\cos\sqrt{6}W \quad (16)$$

$$W=\frac{S_{ij}S_{jk}S_{ki}}{\tilde{S}^3} \quad (17)$$

$$\tilde{S} = \sqrt{S_{ij}S_{ij}}\ ;\ S_{ij} = \frac{1}{2}\left(\frac{\partial u_j}{\partial x_i} + \frac{\partial u_i}{\partial x_j}\right) \quad (18)$$

On the other hand, Eq. 19 and Eq. 20 define the flow velocity (V) as follows:

$$V \equiv \sqrt{S_{ij}S_{ij} + \tilde{\Omega}_{ij}\tilde{\Omega}_{ij}} \quad (19)$$

$$\tilde{\Omega}_{ij} = \overline{\Omega_{ij}} - \varepsilon_{ij}k\omega_k \quad (20)$$

The solution of the terms based on the Reynolds stress tensor supports the CFD model analyzing the relation between the pressure contours, the airflow velocity, and the viscous dissipation rate. In this way, it is possible to apply 5 differential equations to develop a 2D flow analysis and reduce the computational resources of the numerical simulation under VAWT flow conditions used in the CFD model.

3.4 Standard k-ω model

The mathematical modifications model the compressibility effects and determines the Standard k-ω equations to calculate the main properties of turbulent flows. The standard k-ω is an empirical model based on the turbulent kinetic energy (k) and the specific dissipation rate (ω) demonstrated from the Wilcox k-ω model. Eq. 21 and Eq. 22 are the partial differential equations computed to calculate k and ω respectively:

$$\frac{\partial}{\partial t}(\rho k) + \frac{\partial}{\partial x_i}(\rho k u_i) = \frac{\partial}{\partial x_j}\left[\Gamma_k \frac{\partial k}{\partial x_j}\right] + G_k \quad (21)$$

$$\frac{\partial}{\partial t}(\rho \omega) + \frac{\partial}{\partial x_i}(\rho \omega u_i) = \frac{\partial}{\partial x_j}\left[\Gamma_\omega \frac{\partial \omega}{\partial x_j}\right] + G_\omega \quad (22)$$

where G_k represents theturbulent kinetic energy generation in function of the mean velocity gradients and G_ω determines the generation of the specific dissipation rate. Γ defines the effective diffusivity of k and ω by means of the Eq. 23.

$$\Gamma_{k,\omega} = \mu + \frac{\mu_t}{\sigma_{k,\omega}} \quad (23)$$

For the standard k-ω model, μ_t is equal to $\rho k/\omega$ and G_ω is given by the relation $\omega G_k/k$.

3.5 Shear Stress Transport (SST k-ω) model

The SST k-ω model improves the accuracy of the k-ω model in the near-wall region of the computational domain by means of the application of the k-ε model in the far field zone. SST k-ω differs to the standard k-ω model in the application of the damped cross-diffusion term to calculate ω. Eq. 24 shows the difference with an additional term.

$$\frac{\partial}{\partial t}(\rho \omega) + \frac{\partial}{\partial x_i}(\rho \omega u_i) = \frac{\partial}{\partial x_j}\left[\Gamma_\omega \frac{\partial \omega}{\partial x_j}\right] + G_\omega + D_\omega \quad (24)$$

where D_ω is based on the blend of the standard k-ε and the standard k-ω model. The Eq. 25 defines the cross-diffusion value in function of k and ω terms as follows:

$$D_\omega = 2(1 - F_1)\rho \frac{1}{\omega \sigma_{\omega,2}} \frac{\partial k}{\partial x_j}\frac{\partial \omega}{\partial x_j} \quad (25)$$

The Eq. 26 and Eq. 27 determine the first blending function F1 considering the physical values k, ω, and ρ. This additional term proposes an improvement in the accuracy of the SST k-ω for viscous and compressible flows as follows:

$$F_1 = \tanh\left(\min\left[\max\left(\frac{\sqrt{k}}{0.09\omega y}, \frac{500\mu}{\rho y^2 \omega}\right), \frac{4\rho k}{\sigma_\omega, 2D_\omega^+ y^2}\right]\right) \quad (26)$$

$$D_\omega^+ = \max\left[2\rho \frac{1}{\sigma_\omega, 2}\frac{1}{\omega}\frac{\partial k}{\partial x_j}\frac{\partial \omega}{\partial x_j}, 10^{-10}\right] \quad (27)$$

On the other hand, the turbulent viscosity μ_t is a dependent value of k, ω and the blending function F_2, as shown in the Eq 28.

$$\mu_t = \frac{a_1 k}{\max(a_1\omega, \Omega F_2)} \quad (28)$$

Ω is the absolute value of the vorticity and a_1 is equal to 0.3.Eq. 29presents the blending function F_2, as follows:

$$F_2 = \tanh\left(\max\left(2\frac{\sqrt{k}}{0.09\omega y}; \frac{400\mu}{y^2\omega}\right)^2\right) \quad (29)$$

The SST k-ω model considers a set of constant values in Fluent to compute the airflow and analyze its properties into the computational domain: $\sigma_k = 0.85$, $\sigma_\omega = 0.65$, $\kappa = 0.41$, $\beta_1 = 0.0750$, $\beta = 0.09$, and $y = {\beta_1}/{\beta} - \sigma_\omega \kappa^2/\sqrt{\beta}$.

3.6 Generalized (GEKO) k-ω model

Generalized (GEKO) model is a two-equation model based on the standard k-ω model formulation and the possibility to set the main parameters over a wide range of CFD situations for wall bounded flows, free shear flows and corner separation flows with a curvature correction term. A started point for k and ω terms can be expressed by the Eq. 30 and Eq. 31 respectively.

$$\frac{\partial}{\partial t}(\rho k) + \frac{\partial}{\partial x_j}(\rho k u_j) = P_k - C_\mu \rho \omega k + \frac{\partial}{\partial x_j}\left[\Gamma_k \frac{\partial k}{\partial x_j}\right] \quad (30)$$

$$\frac{\partial}{\partial t}(\rho \omega) + \frac{\partial}{\partial x_j}(\rho \omega u_j) = C_{\omega 1} F_1 \frac{\omega}{k} P_k - C_{\omega 2} F_2 \rho \omega^2 + \rho F_3 CD + \frac{\partial}{\partial x_j}\left[\Gamma_\omega \frac{\partial \omega}{\partial x_j}\right] \quad (31)$$

The free GEKO coefficients and the functions (F_1, F_2, F_3) were defined by the user to improve the accuracy during the numerical simulation. Considering the above, Eq. 32 and Eq. 33 determine the turbulent viscosity μ_t and P_k term as follows:

$$\mu_t = \rho \frac{k}{\max\left(\omega, \frac{S}{C_{Realize}}\right)} \quad (32)$$

$$P_k = -\tau_{ij}\frac{\partial u_i}{\partial x_j} \quad (33)$$

Finally, CD and S are the dependent values of the GEKO model supported by the turbulent kinetic energy (k), the specific dissipation rate (ω) and the mean strain rate tensor, respectively. These values are expressed in the Eq. 34 and the Eq. 35.

$$\mathbf{CD} = \frac{\mathbf{2}}{\boldsymbol{\sigma_\omega}}\frac{\mathbf{1}}{\boldsymbol{\omega}}\frac{\boldsymbol{\partial k}}{\boldsymbol{\partial x_j}}\frac{\boldsymbol{\partial \omega}}{\boldsymbol{\partial x_j}} \quad (34)$$

$$\mathbf{S} = \sqrt{\mathbf{2S_{ij}S_{ij}}}\ ;\ \mathbf{S_{ij}} = \frac{\mathbf{1}}{\mathbf{2}}\left(\frac{\boldsymbol{\partial u_i}}{\boldsymbol{\partial x_j}} + \frac{\boldsymbol{\partial u_j}}{\boldsymbol{\partial x_j}}\right) \quad (35)$$

3.7 Baseline k-ω model

The Baseline (BSL) k-ω model derives from the SST model and the Jhonson-King (JK) formulation including the effects of the adverse pressure gradient and the effect of the inertia into a transport equation, this formulation presents accurate results for a large variety of flow problems. The principal shear-stress is proportional to the turbulent kinetic energy to guarantee the agreement between the Eq. 36 and Eq. 37.

$$\frac{\partial}{\partial t}(\rho k) + \frac{\partial}{\partial x_j}(\rho k u_j) = P_k - \beta\rho\omega k + \frac{\partial}{\partial x_j}\left[(\mu + \sigma_k\mu_t)\frac{\partial k}{\partial x_j}\right] \quad (36)$$

$$\frac{\partial}{\partial t}(\rho\omega) + \frac{\partial}{\partial x_j}(\rho u_j\omega) = \gamma P_\omega - \gamma P_{\omega^2} +$$

$$2(1-F_1)\sigma_{\omega^2}\frac{\mu_t}{k}\frac{\partial k}{\partial x_j}\frac{\partial \omega}{\partial x_j} + \frac{\partial}{\partial x_j}\left[(\mu + \sigma_k\mu_t)\frac{\partial k}{\partial x_j}\right] \quad (37)$$

where:

$$P_k = \mu_t\frac{\partial u_i}{\partial x_j}\left(\frac{\partial u_i}{\partial x_j} + \frac{\partial u_j}{\partial x_i}\right) - \frac{2}{3}\rho k S_{ij}\frac{\partial u_i}{\partial x_j} \quad (38)$$

$$P_\omega = \rho\frac{\partial u_i}{\partial x_j}\left(\frac{\partial u_i}{\partial x_j} + \frac{\partial u_j}{\partial x_i}\right) - \frac{2}{3}\rho\omega S_{ij}\frac{\partial u_i}{\partial x_j} \quad (39)$$

The function F_1 is calculated from the Eq. 40, as follows:

$$F_1 = \tanh(\arg_1^4) \quad (40)$$

$$\arg_1 = \max\left(\min\left(\frac{\sqrt{k}}{0.09\omega y}; 0.45\frac{\omega}{\Omega}\right); \frac{400\nu}{z^2\omega}\right) \quad (41)$$

where z is the distance to the next surface and the eddy viscosity is computed by the solver as: $\nu_t = {}^{k}/_{\omega}$.

4. Methodology

The complex behavior of the turbulent flow and the influence of the airfoil geometry were analyzed to determine the NACA 0012 performance with a CFD approach. In this sense, the CFD methodology defined the numerical data of the flow around the airfoil and the main fluctuations presented by the pressure gradients of the airflow [28].

4.1 Boundary conditions

The boundary conditions of the numerical model arethe velocity inlet and the pressure output computed to calculate the influence of the airfoil geometry witha range of angle of attack from 0º to 90º. Then, the fluctuations of the turbulent flow can be studied in function of the airflow features and the turbulent kinetic energy contours to analyze the transferred energy around the surfaces of the NACA 0012 airfoil. An incompressible flow was modeled with the computing of the Mach number equal to 0.6.

The constant value of the air density equal to 1.225 kg/m^{3}close to the walls of the computational domain defined the pressure-based solver to calculate the incompressible flow during the processing of the discretized equations. Then, the experimental data was compared with the pressure coefficient of the NACA 0012 airfoil considering the physical effects produced by the airfoil interaction. Table 1 shows the features of the CFD model developed with ANSYS to model the airflow around the airfoil.

Table 1: Parameters of the CFD study

Parameter	Operational data
Velocity inlet 1	1 m/s
Velocity inlet 2	5 m/s
Pressure outlet	760 mmHg
Angle attack	0º to 90º
Airflow density	1.225 kg/m^3
Mach number	0.6

4.2 Mesh independence study

The mesh independence study defined the finite number of cells to reach a good behavior of the residuals generated during the solution of the differential equations system using a second-order scheme with ANSYS software. The numerical results were analyzed according to the mesh dependence study developed byLe et al. [29], where the numerical simulation defines the lift and drag coefficients of the airfoil for an AoA equal to 0º. In the first step, the standard k-ε turbulence model supports the numerical model considering five different meshes to study the influence of the cells in the numerical accuracy of the flow simulated around the airfoil surfaces. Fig. 2 shows the mesh applied to create a discrete decomposition of the geometry to process the conservation equations and visualize the flow [30].

Figure 2: Structured mesh of the computational domain

Hexahedral cells are widely used in CFD studies due to the high accuracy needed to simulate the turbulent flow. This approach generates a better flow simulation near to the

complex surfaces of the airfoil. The mesh configuration is based on the statistical parameters that determine the quality of the pressure and velocity contours in the computational domain: the skewness, orthogonal quality, and aspect ratio presented in Table 2[29].

Table 2: Mesh quality of Numerical model

Variable	Statistic value	Mesh criteria
Aspect ratio	2.461	Acceptable
Orthogonal quality	0.992	Convergence
Skewness	0.810	Convergence

Adaptive meshing techniques boosted the accuracy in the numerical definition of the turbulent flow parameters with the effect of the zero AoA with an airfoil thickness equal to12% of the chord length. The quantity of computational resources needed to solve the conservation equations in the set of cells and points that conform the mesh and the numerical errors generated by the quality of the discretized computational domain were reduced. Fig. 3illustrates the mesh independency study based on the numerical results to select 12250 nodes in the model.

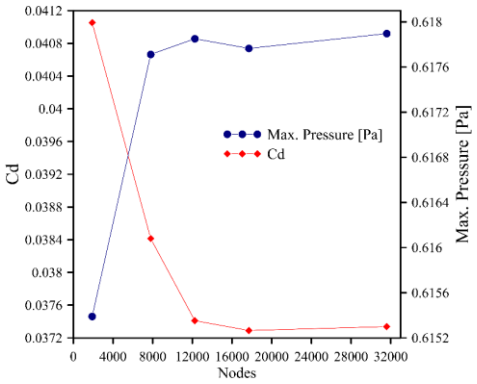

Figure 3: Mesh independency study. AoA=0º; Re=17600.

5. Results

In this section of the CFD study, the comparison of the turbulence models determined the accuracy in the solution of the partial differential equations considering the calculation of the lift component which determine the forces associated to the motion of the airfoil maintaining a perpendicular direction. On the other hand, the drag component determines the kinetic energy losses and the inertial forces directly opposed to the motion of the airfoil. These aerodynamic forces tend to change with the variation of the atmospheric conditions, including the wind velocity and the air density. Then, the performance coefficients versus the AoA are calculated with the CFD model.

5.1 Numerical model validation

The numerical solution of the conservation equations with the CFD algorithm determined the turbulence effects associate to the flow displaced around the surfaces of the airfoil [31]. The improvement of these computational codes depends on the application of the differential equations computed to develop a practical solution of the engineering problems for separated flows or flows with multiple length scales.

The convergence of the residual values during the numerical simulation demonstrated an adequate application of the second-order scheme to process the two equations models and determine variables modeled in the virtual environment. Fig. 4 shows the behavior of the residual values with the application of the RANS model in the computational algorithm processed with Fluent.

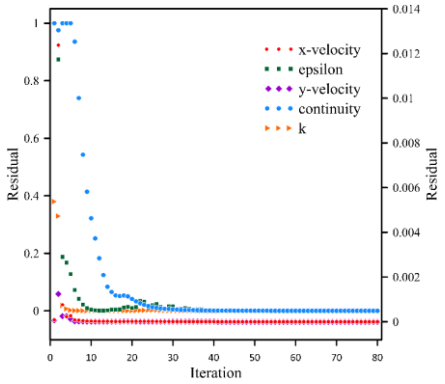

Figure 4: Convergence of the SKE turbulence model

The numerical model analyzed the lift, drag and pitching-moment coefficients computing seven turbulence models with a chord length equal to 1 meter for a Re equal to 17600 and 32600.Fig. 5 shows the convergence of the performance coefficients after 50 iterations for AoA=0º to verify the lift-to-drag ratio and determine the VWAT performance for an AoA from 0º to 90º.

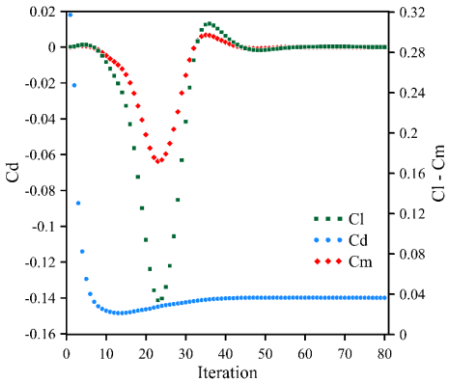

Figure 5: Calculation of the performance coefficients

On the other hand, Fig. 6 shows the calculation of the pressure coefficient and the good agreement between the experimental data and the numerical results of the CFD model. In this way it is possible to simulate the variability of the environmental conditions and define different aerodynamic profiles to analyze a set of wing sections and guarantee an optimal calculation of the flow properties.

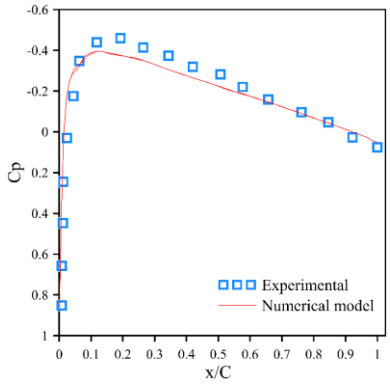

Figure 6: Numerical model validation

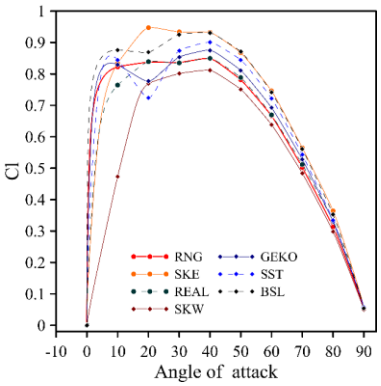

Figure 8: Lift coefficient. Re=17600.

5.2 Performance coefficients of the airfoil

The comparative study of the turbulence models defines the lift, drag, and pitching-moment coefficients of the NACA 0012 considering the effects of the flow separation which influence the lift to drag ratio and the VAWT performance.

Two constant flow regimes were selected to simulate the flow around the surfaces of the airfoil: 17600 and 35200 associating the vortex generation close to the airfoil surfaceto the variations of the pressure gradientsbetween0º to 90º AoA. The Eq. 42, Eq. 43, and Eq. 44 define the drag, lift and pitching-moment coefficients of the airfoil, respectively.

$$D = {}^{1}/_{2}\,\rho V^{2} S C_{D} \quad (42)$$

$$L = {}^{1}/_{2}\,\rho V^{2} S C_{L} \quad (43)$$

$$M = {}^{1}/_{2}\,\rho V^{2} S C_{M} \quad (44)$$

Fig. 7 shows the drag coefficient of the airfoil associated to the Re=17600, where the turbulence models describe an increase of the energy losses as the AoA of the airfoil increases. Unlike the Fig. 8, where the lift coefficient decreases from the AoA equal to 40º due to the reduction of the pressure gradients between the high and low airfoil surface which influence the flow wake generation along the NACA 0012 airfoil.

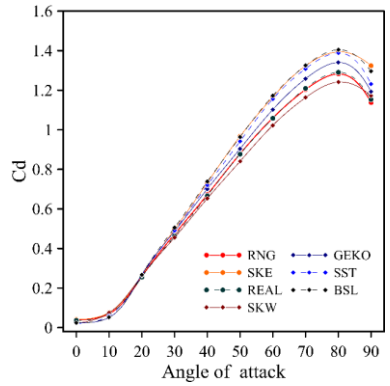

Figure 7: Drag coefficient. Re=17600.

On the other hand, Fig. 9 presents the calculation of the pitching moment coefficient for each turbulence model. A low variation of the Cm until 20º AoA is reached by the turbulence models. However, the variation of the Cm for greater AoA relates the calculation of the pressure gradients with the definition of the angular moment generated by the airfoil.

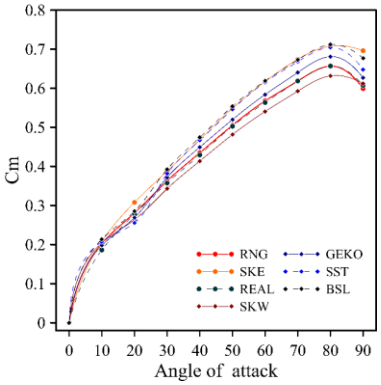

Figure 9: Pitching-moment coefficient. Re=17600.

Fig. 10 shows the effects of the inertial forces associated to the free airflow and their interaction with the inclined airfoil. The aerodynamic efficiency depends on the relation between the minimum drag coefficient and the maximum lift coefficient produced by the pressure gradients and the reaction of the down free airflow displaced under the airfoil surface. Therefore, it can be seen the peak of the lift-to-drag ratio equal to 16 for AoA values less than 20º and the approximation of the GEKOKW and BSLKW models associated to the detection of the lift forces in the airfoil surface for a Re equal to 17600.

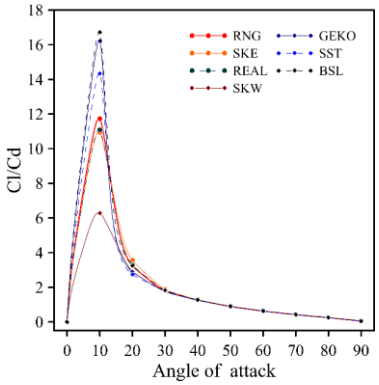

Figure 10: Lift-to-dragratio.Re=17600.

Fig. 11 and Fig. 12 shows the drag and lift coefficients of the airfoil modeled with the Re equal to 35200, respectively. The numerical results showed a low variability of the drag coefficient until the AoA equal to 30º due to the better flow prediction reached by the RANS k-ε models for a higher flow regime. In contrast to the k-ω models, where a better numerical modelling of the flow displaced is reached for low or high flow regimes.

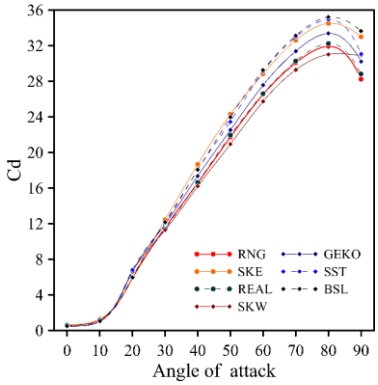

Figure 11: Drag coefficient.Re=35200.

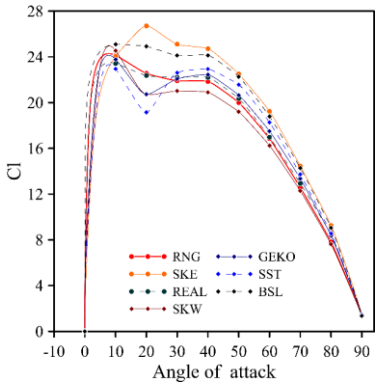

Figure 12: Lift coefficient. Re=35200.

The high variation of the lift coefficient may be associated to the airflow fluctuations and the pressure gradient associated to the vortex detachment phenomena. On the other hand, the two equation models detected a similar behavior of the pitching-moment coefficient for both flow regimes. However, it is important to note the influence of the turbulence effects near to the surfaces of the airfoil. High pitching-moment values (Fig. 13) were associated to the inclination of the airfoil and the inertial forces produced by the interaction of the free streamlines modeled with ANSYS software.

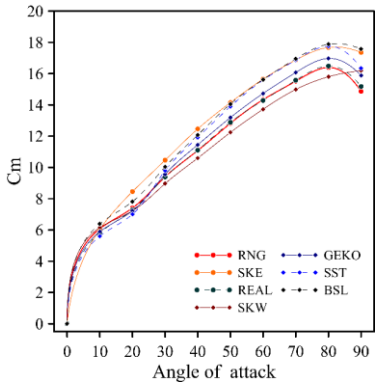

Figure 13: Pitching-moment coefficient. Re=35200.

Thek-ω turbulence models developed a similar behavior in the analysis of the performance coefficients modeled with Re equal to 35200. Considering the above,SKW and SSTKW models can improve the prediction of the lift-to-drag ratio (Fig. 14) in the flow simulationwith a high Re value.On the other hand, the turbulence models GEKO and BSL detected a peak value associated to the AoA equal to 10º.

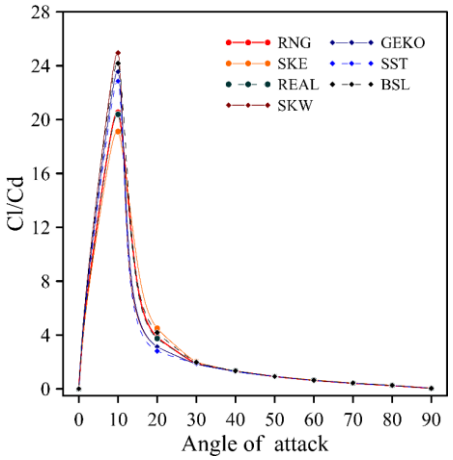

Figure 14: Lift-to-drag coefficient.Re=35200.

5.3 Visualization of the NACA 0012-airflow interaction

In this section, the CFD model visualize the contours of the pressure, velocity, and the turbulent kinetic energy of the airflow from 0º to 90º AoA after to solve the NS equations with the segregated solver. These numerical results show the effects of the pressure gradients on the vortex detachment phenomena and the flow wake generation near to the surfaces of the airfoil.

The contours of the turbulent kinetic energy for an AoA=20º present the flow instabilities influenced by the pressure gradients of the streamlines. The turbulence models SKW, GEKOKW, BSLKW, and SKE developed a good vortex visualization with a flow regime equal to 17600, as shown in the Fig. 15.

However, the CFD results improved in the flow simulation with a Re equal to 35200. In this sense, SKW, BSLKW, GEKOKW, SKE, and RKE presented a remarkable difference in the visualization of the boundary layer detachment, as shown in the Fig. 16.

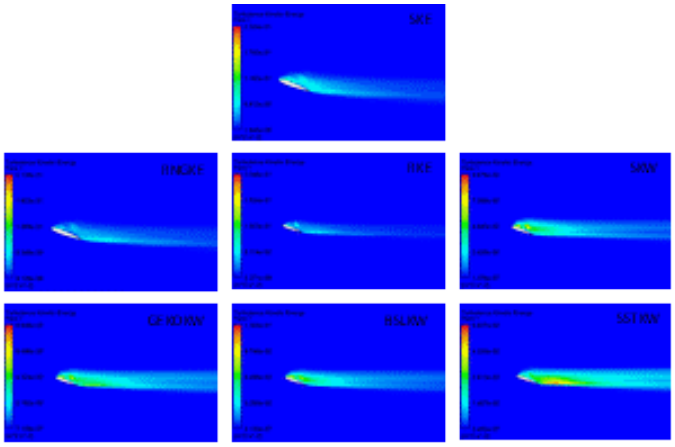

Figure 15: Turbulent kinetic energy with AoA=20°, Re=17600.

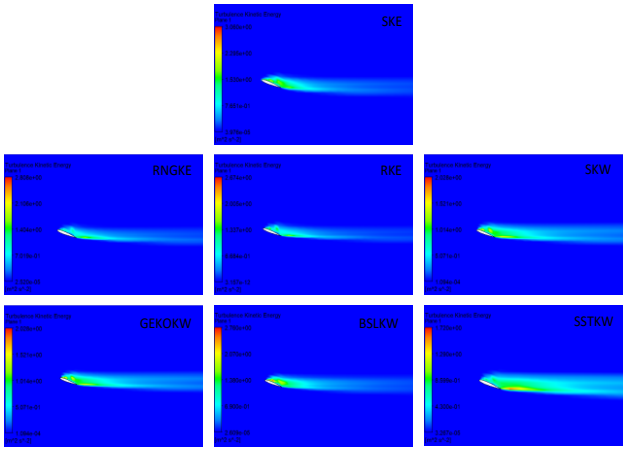

Figure 16: Turbulent kinetic energy with AoA=20°, Re=32500.

The main instabilities of the flow were associated to the pressure gradients near to the surface of the airfoil. Fig. 17 presents the pressure contours of the airflow considering a Re equal to 17600. The SKW turbulence model detected the vortex detachment phenomenon with a modeling of the Re number equal to 17600. SKW demonstrated the numerical prediction of the viscous effects and its strong relation with the pressure gradients which influence the vortex generation on the airfoil.

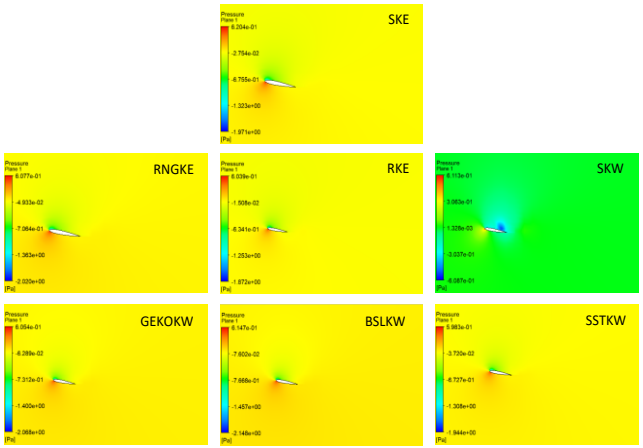

Figure 17: Airflow pressure with AoA=20°, Re=17600.

The CFD results in the Fig 18 showed the influence of the AoA on the flow wake generation near to the surfaces of the airfoil and the formation of the boundary layer which cover the presented void. Similar simulation results of the streamline patterns and the separation of the vortex is presented by Almutairi et al. [31] where the vortex generation and the flow wake production are observed in a transient state simulation for an AoA equal to 9º and Re equal to 13000.

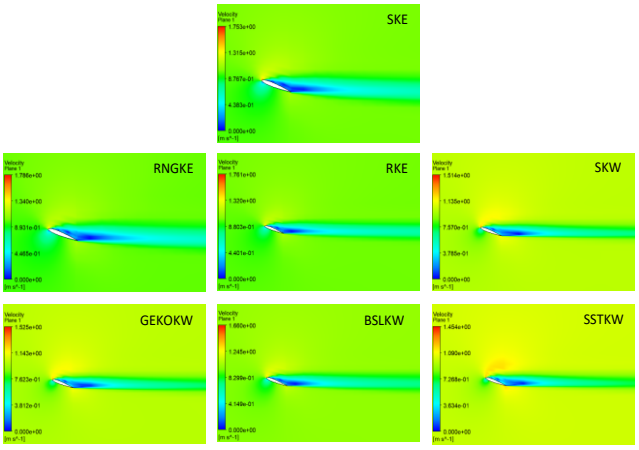

Figure 18: Lift-to-drag coefficient. Re=17600.

6. Conclusions

In this study, RANS k-ε and RANSk-ω models were configured by using 12250 nodes to conform the control volume. This numerical approach defined a hexahedral grid structure into the virtual space. The mesh refinement technique improved the visualization of the turbulent flow close to the NACA 0012 surfaces, as presented in the similar study developed by Mansour et al. [32]where the impact of the hexahedral mesh application and the shortest convergence reached during the partial differential equations processing is demonstrated.

The analysis of the airfoil coefficients used to study the airflow interaction and the airfoil geometry in a virtual environment enables the application of complex algorithms and CFD tools capable of visualize the turbulence produced by the turbulent kinetic energy in space and time. A peak of lift-to-drag ratio was observed for an AoA equal to 10º. However, it is possible to develop CFD studies focused in the environmental conditions and the cambered form of the airfoil used to predict the effects of the flow displaced around the complex geometry of the airfoil determining the aerodynamic efficiency of VAWT in a range of 0º to 90º AoA.

A computational mesh conformation supported the processing of the Navier – Stokes equations computing a finite set of numerical iterations considering an application of the second scheme into the segregated solver to boost the convergence criteria. The maximal skewness value equal to 0.81 computed a suitable mesh generation to reduce divergence errors during the model solution. A stable convergence criterion was reached from 50 iterations of the numerical model.

The velocity, pressure, and turbulent kinetic energy

contours were analyzed and compared with the performance coefficients of the airfoil. The numerical definition of the performance coefficients established the lift-to-drag ratio for the better working condition of the NACA 0012 into the 2D domain, with a better predictability reached by SKW, BSLKW, GEKOKW and SKE turbulence models.

7. Acknowledgement

The Authors like to acknowledge the Universidad del Atlántico and Prenteck Ingeniería for their support in the development of this research.

References

[1] E. M. Serino Monteiro, L. Lima Monteiro, and J. A. Peixoto da Costa, "CFD Simulation of Pneumatic Valve for Energy Efficiency Studies," *International Journal of Science and Research (IJSR)*, vol. 11, no. 2, pp. 195–198, Feb. 2022.

[2] V. Venkkatrami Reddy and K. Srinivasa Rao, "Design and Fabrication of Vertical Axis Wind Mill Turbine," *International Journal of Science and Research (IJSR)*, vol. 7, no. 1, pp. 403–406, Jan. 2018.

[3] Mohd Islam and Misba Jan, "Review of Fluid Flow and Heat Transfer through Microchannels," *International Journal of Science and Research (IJSR)*, vol. 5, no. 4, pp. 1421–1425, Apr. 2016.

[4] J. U. Parakkal, K. el Kadi, A. El-Sinawi, S. Elagroudy, and I. Janajreh, "Numerical analysis of VAWT wind turbines: Joukowski vs classical NACA rotor's blades," *Energy Procedia*, vol. 158, pp. 1194–1201, 2019, doi: https://doi.org/10.1016/j.egypro.2019.01.306.

[5] S. Gururatana, R. Prapainop, S. Chuepeng, and S. Skullong, "Development of heat transfer performance in tubular heat exchanger with improved NACA0024 vortex generator," *Case Studies in Thermal Engineering*, vol. 26, p. 101166, Aug. 2021, doi: 10.1016/j.csite.2021.101166.

[6] W. Yossri, S. ben Ayed, and A. Abdelkefi, "Airfoil type and blade size effects on the aerodynamic performance of small-scale wind turbines: Computational fluid dynamics investigation," *Energy*, vol. 229, p. 120739, 2021, doi: https://doi.org/10.1016/j.energy.2021.120739.

[7] A. Kulshreshtha, S. K. Gupta, and P. Singhal, "FEM/CFD analysis of wings at different angle of attack," *Materials Today: Proceedings*, vol. 26, pp. 1638–1643, 2020, doi: https://doi.org/10.1016/j.matpr.2020.02.342.

[8] A. Eltayeb, S. Tan, Z. Qi, A. A. Ala, and Nisrene. M. Ahmed, "PLIF experimental validation of a FLUENT CFD model of a coolant mixing in reactor vessel down-comer," *Annals of Nuclear Energy*, vol. 128, pp. 190–202, 2019, doi: https://doi.org/10.1016/j.anucene.2018.12.051.

[9] A. A. G. Maia, J. S. Kapat, J. T. Tomita, J. F. Silva, C. Bringhenti, and D. F. Cavalca, "Preconditioning methods for compressible flow CFD codes: Revisited," *International Journal of Mechanical Sciences*, vol. 186, p. 105898, 2020, doi: https://doi.org/10.1016/j.ijmecsci.2020.105898.

[10] V. Puoti, "Preconditioning Method for Low-Speed Flows," *AIAA Journal*, vol. 41, no. 5, pp. 817–830, May 2003, doi: 10.2514/2.2043.

[11] L. M. Meyers and V. Msomi, "Hydrodynamic analysis of an underwater glider wing using ANSYS fluent as an investigation tool," *Materials Today: Proceedings*, vol. 45, pp. 5456–5461, 2021, doi: https://doi.org/10.1016/j.matpr.2021.02.127.

[12] S. Kumar, R. K. Das, and K. Kulkarni, "Comparative study of solar air heater (SAH) roughened with transverse ribs of NACA 0020 in forward and reverse direction," *Case Studies in Thermal Engineering*, p. 102015, 2022, doi: https://doi.org/10.1016/j.csite.2022.102015.

[13] S. Mondal and R. W. Field, "Theoretical analysis of the viscosity correction factor for heat transfer in pipe flow," *Chemical Engineering Science*, vol. 187, pp. 27–32, 2018, doi: 10.1016/j.ces.2018.04.047.

[14] G. J. Brown, D. F. Fletcher, J. W. Leggoe, and D. S. Whyte, "Application of hybrid RANS-LES models to the prediction of flow behaviour in an industrial crystalliser," *Applied Mathematical Modelling*, vol. 77, pp. 1797–1819, 2020, doi: https://doi.org/10.1016/j.apm.2019.09.032.

[15] D. Liu and T. Nishino, "Numerical analysis on the oscillation of stall cells over a NACA 0012 aerofoil," *Computers & Fluids*, vol. 175, pp. 246–259, 2018, doi: https://doi.org/10.1016/j.compfluid.2018.08.016.

[16] S. Heinz, "A review of hybrid RANS-LES methods for turbulent flows: Concepts and applications," *Progress in Aerospace Sciences*, p. 100597, 2020, doi: https://doi.org/10.1016/j.paerosci.2019.100597.

[17] T. K. Sengupta, A. Bhole, and N. A. Sreejith, "Direct numerical simulation of 2D transonic flows around airfoils," *Computers & Fluids*, vol. 88, pp. 19–37, 2013, doi: https://doi.org/10.1016/j.compfluid.2013.08.007.

[18] Autodesk, "Autodesk Simulation CFD External Flow Validation: NACA 0012 Airfoil," in *Review NACA0012 2D*, 2015, p. 14.

[19] G. Bellakhal Ghazi Bellakhal, F. Chaibina, and J. Chahed, "Assessment of turbulence models for bubbly flows: toward a Five-Equation turbulence model," *Chemical Engineering Science*, p. 115425, Dec. 2019, doi: 10.1016/J.CES.2019.115425.

[20] A. Bayon, D. Valero, R. García-Bartual, F. J. Vallés-Morán, and P. A. López-Jiménez, "Performance assessment of OpenFOAM and FLOW-3D in the numerical modeling of a low Reynolds number hydraulic jump," *Environmental Modelling and Software*, vol. 80, pp. 322–335, 2016, doi: 10.1016/j.envsoft.2016.02.018.

[21] J. Sánchez, J. Duarte, and G. Valencia, "RANS simulations of the flow in a centrifugal fan using OpenFOAM," *International Review on Modelling and Simulations*, 2019.

[22] M. Tiberga, A. Hennink, J. L. Kloosterman, and D. Lathouwers, "A high-order discontinuous Galerkin solver for the incompressible RANS equations coupled to the k−ϵ turbulence model," *Computers & Fluids*, vol. 212, p. 104710, 2020, doi: https://doi.org/10.1016/j.compfluid.2020.104710.

[23] W. P. Jones and B. Launder, "The prediction of

laminarization with a two-equation model of turbulence," *International Journal of Heat and Mass Transfer*, vol. 15, pp. 301–314, Feb. 1972, doi: 10.1016/0017-9310(72)90076-2.

[24] M. Tabib, M. S. Siddiqui, A. Rasheed, and T. Kvamsdal, "Industrial scale turbine and associated wake development-comparison of RANS based Actuator Line Vs Sliding Mesh Interface Vs Multiple Reference Frame method.," *Energy Procedia*, vol. 137, pp. 487–496, 2017, doi: 10.1016/j.egypro.2017.10.377.

[25] A. Buffo, M. Vanni, and D. L. Marchisio, "On the implementation of moment transport equations in OpenFOAM: Boundedness and realizability," *International Journal of Multiphase Flow*, vol. 85, pp. 223–235, 2016, doi: 10.1016/j.ijmultiphaseflow.2016.06.017.

[26] N. N. Mansour and A. A. Wray, "Decay of isotropic turbulence at low Reynolds number," *Physics of Fluids*, vol. 6, no. 2, pp. 808–814, Feb. 1994, doi: 10.1063/1.868319.

[27] A. Escue and J. Cui, "Comparison of turbulence models in simulating swirling pipe flows," *Applied Mathematical Modelling*, vol. 34, no. 10, pp. 2840–2849, 2010, doi: https://doi.org/10.1016/j.apm.2009.12.018.

[28] A. S. Rezaei and H. Taha, "Circulation dynamics of small-amplitude pitching airfoil undergoing laminar-to-turbulent transition," *Journal of Fluids and Structures*, vol. 100, p. 103177, 2021, doi: https://doi.org/10.1016/j.jfluidstructs.2020.103177.

[29] N. T. P. Le, A. Shoja-Sani, and E. Roohi, "Rarefied gas flow simulations of NACA 0012 airfoil and sharp 25–55-deg biconic subject to high order nonequilibrium boundary conditions in CFD," *Aerospace Science and Technology*, vol. 41, pp. 274–288, 2015, doi: https://doi.org/10.1016/j.ast.2014.12.019.

[30] W. Wang, Y. Cao, and T. Okaze, "Comparison of hexahedral, tetrahedral and polyhedral cells for reproducing the wind field around an isolated building by LES," *Building and Environment*, vol. 195, p. 107717, 2021, doi: https://doi.org/10.1016/j.buildenv.2021.107717.

[31] J. AlMutairi, E. ElJack, and I. AlQadi, "Dynamics of laminar separation bubble over NACA-0012 airfoil near stall conditions," *Aerospace Science and Technology*, vol. 68, pp. 193–203, 2017, doi: https://doi.org/10.1016/j.ast.2017.05.015.

[32] M. Mansour, P. Khot, P. Kováts, D. Thévenin, K. Zähringer, and G. Janiga, "Impact of computational domain.